THE JOURNAL OF PHYSICAL CHEMISTRY LETTERS
A JOURNAL OF THE AMERICAN CHEMICAL SOCIETY

pubs.acs.org/JPCL

Letter

Atomic Reconstruction and Oxygen Evolution Reaction of Mn_3O_4 Nanoparticles

Sangmoon Yoon, Hongmin Seo, Kyoungsuk Jin, Hyoung Gyun Kim, Seung-Yong Lee, Janghyun Jo, Kang Hee Cho, Jinseok Ryu, Aram Yoon, Young-Woon Kim, Jian-Min Zuo, Young-Kyun Kwon, Ki Tae Nam, and Miyoung Kim*

Cite This: *J. Phys. Chem. Lett.* 2022, 13, 8336–8343

Read Online

ACCESS | Metrics & More | Article Recommendations | Supporting Information

ABSTRACT: Understanding the chemical states of individual surface atoms and their arrangements is essential for addressing several current issues such as catalysis, energy stroage/conversion, and environmental protection. Here, we exploit a profile imaging technique to understand the correlation between surface atomic structures and the oxygen evolution reaction (OER) in Mn_3O_4 nanoparticles. We image surface structures of Mn_3O_4 nanoparticles and observe surface reconstructions in the (110) and (101) planes. Mn^{3+} ions at the surface, which are commonly considered as the active sites in OER, disappear from the reconstructed planes, whereas Mn^{3+} ions are still exposed at the edges of nanoparticles. Our observations suggest that surface reconstructions can deactivate low-index surfaces of Mn oxides in OER. These structural and chemical observations are further validated by density functional theory calculations. This work shows why atomic-scale characterization of surface structures is crucial for a molecular-level understanding of a chemical reaction in oxide nanoparticles.

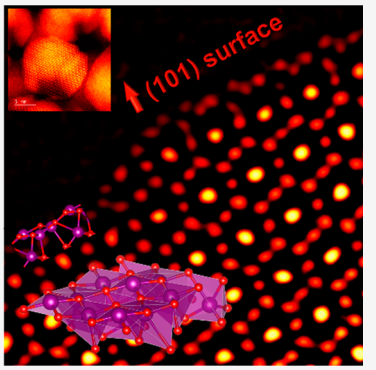

Surface chemistry and reactions are fundamental to the properties of various functional materials, including solid catalysts, supercapacitors, and sensors.[1] At the molecular level, surface atoms interact differently with surrounding molecules depending on their local atomic arrangements, such as facet, step, edge, and corner atoms, and surface defects, causing considerable variations in the chemical environment.[2] Furthermore, surface relaxation and reconstruction also significantly alter chemical reactions at the surface because of modified electronic structures. Together, surface atomic arrangements and surface reconstructions constitute what is broadly defined as surface structures. Because of the complexity of surface structures, atomic-level characterization is essential for a molecular-level understanding of surface chemical reactions. For example, identification of the active sites among various surface atoms in catalysis can lead to direct advances in catalyst design.[3] While a variety of advanced surface characterization techniques have been developed and employed to obtain information associated with chemical reactions at specific surface sites, most techniques have their own restrictions for the surface types that can be studied, and accurate measurement of atomic and electronic structures with high precision remains difficult in nanostructured materials.[4]

Surface profile imaging[5,6] by transmission electron microscopy (TEM), particularly scanning transmission electron microscopy (STEM) in combination with electron energy loss spectroscopy (EELS), is a novel technique for the analysis of nanoparticle surfaces. The high-angle annular dark-field (HAADF) mode in STEM allows individual atomic columns to be located, and EELS provides information on the electronic and chemical states simultaneously. Recently, the capability of this technique has improved significantly due to the dramatic advances in aberration correction. Surfaces of the complex metal oxides, as well as simple metals, have been studied using this technique.[7−9] Scanning tunneling microscopy (STM) is another representative technique that directly provides atomic-scale images of surface structures. Indeed, pioneering STM studies have provided a great deal of information regarding surface chemical reactions.[10,11] However, characterizing the nanoparticle surfaces on the atomic scale with STM-based techniques is practically challenging because samples must be atomically flat for atomic-resolution imaging. Scanning transmission X-ray microscopy (STXM) and X-ray absorption spectroscopy (XAS) are X-ray-based techniques analogous to STEM and EELS.[12] STXM/XAS has more degrees of freedom for designing *in situ* environments and dealing with sample damage, but it is difficult to achieve atomic resolution with these methods because of the limited spatial resolution of X-ray probes.[13] Vibrational spectroscopy methods, such as infrared, ultraviolet, and Raman spectroscopy, have also been

Received: May 30, 2022
Accepted: August 26, 2022
Published: August 30, 2022

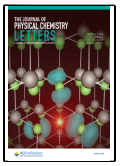

https://doi.org/10.1021/acs.jpclett.2c01638
J. Phys. Chem. Lett. 2022, 13, 8336–8343

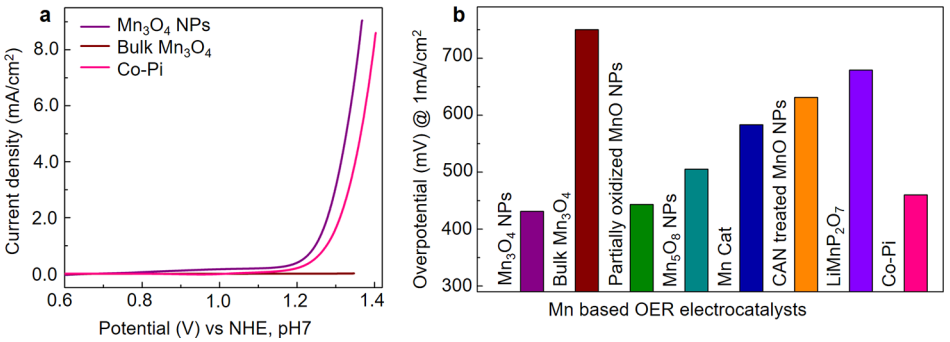

Figure 1. Electrochemical performance of Mn_3O_4 nanoparticles in the oxygen evolution reaction (OER). (a) Polarization-corrected cyclic voltammetry (CV) curve of Mn_3O_4 nanoparticles in the OER. The purple, wine, and magenta solid lines represent Mn_3O_4 nanoparticles, bulk Mn_3O_4, and cobalt phosphate (Co-Pi), respectively. (b) Comparison of the overpotential between the Mn_3O_4 nanoparticles and existing OER catalysts.

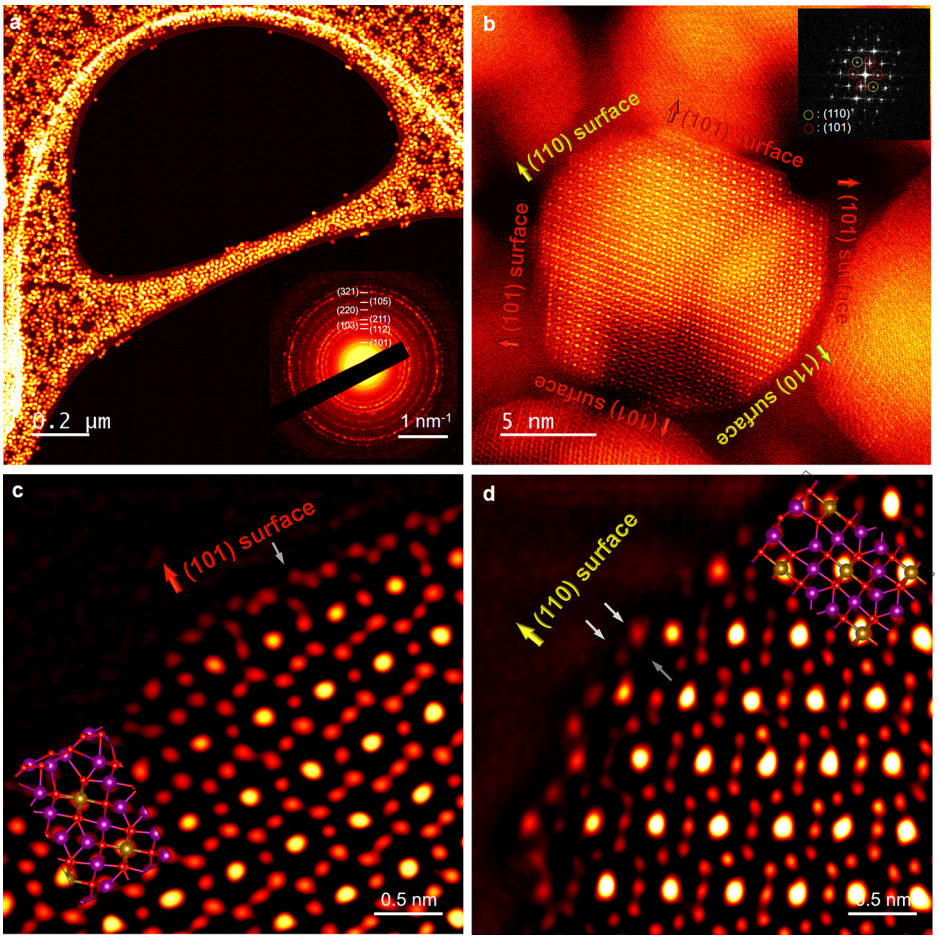

Figure 2. Atomic surface structure of Mn_3O_4 nanoparticles. (a) Low-magnification high-angle annular dark-field (HAADF) scanning transmission electron microscopy (STEM) image of nanoparticles. The inset shows the selected area electron diffraction (SAED) pattern in the image area. (b) High-resolution HAADF STEM image of a nanoparticle viewed along the [111] zone axis. The inset shows the fast Fourier transformation (FFT) pattern of the nanoparticle, where the yellow and red circles indicate the (110) and (101) peaks, respectively. (c,d) High-resolution HAADF STEM image of the (c) (101) facet and (d) (110) facet.

applied extensively for the characterization of surface chemical reactions mostly focused on chemical bonding between absorbed molecules and a surface.[14] Recently, the spatial resolution of these techniques has also improved due to the local enhancement effects near a sharp metal tip, yet, structural information is still limited to the nanometer scale.[15,16] Obviously, STEM-EELS surface profile imaging provides unique information on both the atomic and electronic structures of nanostructure surfaces, which cannot be obtained with other techniques.

Here, atomic surface structure of Mn_3O_4 oxygen evolution nanocatalysts was explored using STEM-EELS surface profile imaging. Manganese (Mn) oxides have attracted a great deal of attention with regard to oxygen evolution reaction (OER), since a Mn oxide cluster was discovered to be a naturally occurring OER catalyst in photosystem II.[17] Extensive efforts

https://doi.org/10.1021/acs.jpclett.2c01638
J. Phys. Chem. Lett. 2022, 13, 8336−8343

have been devoted to the design of an artificial Mn-based OER catalyst. Mn oxides are found to exhibit high activity in a nanoform[18,19] or after a specific surface treatment.[20,21] The functional improvement of Mn oxides is likely related to the surface properties; however, the mechanisms underlying these improvements remain unclear. One clue is that active Mn-based electrocatalysts that exhibit high OER activity commonly contain Mn^{3+} ions on their surfaces. Zaharieva et al. reported that the active catalysts among electrodeposited MnO_x OER catalysts exhibit a structural disorder involving a Mn^{3+} ion.[20] Park et al. presented direct evidence that the Mn^{3+} ion content is strongly correlated with the catalytic activity.[22] With regard to the reaction mechanism, Takashima et al. suggested that stabilization of Mn^{3+} ions during the reaction is crucial for OER.[23,24] In addition to these reports, several studies have demonstrated the appearance of Mn^{3+} ions on the surfaces of Mn-based OER electrocatalysts.[25,26] While the precise role of Mn^{3+} ions in OER is not yet understood, these results suggest that Mn^{3+} ions are strongly coupled to the activity of Mn oxides in the OER. In this context, the high activity of Mn_3O_4 nanocatalysts is a puzzle. Mn_3O_4 contains abundant Mn^{3+} ions, but it is inactive in the micropowder-form and only becomes active when in the nanoform.[19,27]

To determine the structural origin of OER activities on the Mn_3O_4 surfaces, the analysis of the surface atomic configurations and electronic structures of Mn_3O_4 nanoparticles were carried out using STEM-EELS. First, two types of polar surfaces, (110) and (101) surfaces, were frequently observed as the low-index facets of Mn_3O_4 nanoparticles. Importantly, both surfaces were found to undergo surface reconstructions, and Mn^{3+} ions, which are commonly believed to be associated with the active sites, disappeared from the reconstructed surfaces. The thermodynamic stability of reconstructed surfaces and their altered electronic structures was validated by density functional theory (DFT) calculations based on the experimental structural models. Meanwhile, the edges of the nanoparticles were found to contain active Mn^{3+} ions on the surface. Our results suggest that surface reconstruction often makes stable Mn oxide surfaces inactive in OER. This study demonstrates the importance of an atomistic understanding of catalytic surface structures and provides insight into the design of novel functional nanomaterials.

The OER activity of Mn_3O_4 nanoparticles was evaluated by cyclic voltammetry (CV). Figure 1(a) shows the polarization-corrected CV curve of Mn_3O_4 nanoparticles compared to commercial Mn_3O_4 micropowder and a Co-Pi electrocatalyst,[28] which was measured at a pH of 7.0 in a 0.5 M phosphate buffer solution. Mn_3O_4 nanoparticles exhibited a low overpotential of 450 mV at a current density of 1 mA cm^{-2}, comparable to Co-Pi electrocatalysts. Mn_3O_4 micropowder was almost inactive, and an overpotential of 750 mV was required to achieve a current density of 1 mA cm^{-2}. The commercial Mn_3O_4 micropowder is a polycrystalline sample with the grain size of several hundred nanometers. The overpotentials of Mn_3O_4 nanoparticles and other Mn-based OER electrocatalysts are shown in Figure 1(b) for comparison of the OER activities. It shows that the Mn_3O_4 nanoparticle is one of the active Mn-based electrocatalysts operating under neutral conditions. Here, it is noteworthy that 10 nm scale Mn_3O_4 nanoparticles synthesized through different procedures also showed similar OER activity.[29]

Since the catalytic reaction occurs predominantly at the surfaces, it is important to obtain structural information on the surfaces. Figure 2(a) shows a low-magnification HAADF STEM image and the corresponding selected area electron diffraction (SAED) pattern of the Mn_3O_4 nanoparticles. The nanoparticles were monodispersed, with a size of 15 nm, and had a single phase of Mn_3O_4. The nanoparticles that were attached to the side of the lacey carbon mesh without a supporting layer were examined to exclude the scattering from the carbon supporting layer for more accurate measurements. Figure 2(b) shows a high-magnification HAADF STEM image of a Mn_3O_4 nanoparticle viewed along the [111] zone axis, which allows the (110) and (101) surfaces to be examined. The profile image indicates that Mn_3O_4 nanoparticles are faceted nanostructures with (110) and (101) surfaces. Note that (100) surface is another low-index plane that makes up the nanoparticle surfaces (see Figure S1). Several other HAADF STEM images are displayed in the Supporting Information; these show that many nanoparticles are composed of two or three mosaic blocks, but still, nanoparticles were surrounded by (101), (110), and (001) surfaces (see Figure S2).

Atomic surface structures of the (110) and (101) facets were observed at a higher magnification for atomic resolution, as shown in Figure 2(c,d), respectively. Bright dots indicate Mn columns, and their brightness was roughly determined by the density of Mn ions in each atomic column. Meanwhile, oxygen columns were generally not detected in the HAADF STEM images because the HAADF STEM provides the scattering intensity that is approximately proportional to the square of the atomic number.[30,31] The atomic configurations of the surfaces differed significantly in the HAADF STEM images from those observed in the bulk Mn_3O_4, clearly demonstrating that surface reconstruction occurred on each facet of the Mn_3O_4 nanoparticles. In the (101) surface, an additional Mn column always appeared in each period, which is denoted by the gray arrow in Figure 2(c). Meanwhile, in the (110) surface, two Mn columns of the topmost layer of the surface became brighter, and a Mn column in the subsurface layer disappeared. The brightened Mn columns and vanishing Mn column are denoted by the bright- and dark-gray arrows in Figure 2(d), respectively. The appearance of surface reconstructions implies unstable surface planes. Indeed, both (110) and (101) planes exposed on the Mn_3O_4 nanoparticles are polar surfaces with uncompensated electrostatic potential. To note, the surface polarity can be neutralized in various ways such as charge redistribution or interaction with other foreign atoms, in addition to surface reconstruction. Our observations show that the polarity of the (110) and (101) surfaces on Mn_3O_4 nanoparticles was compensated by the surface reconstructions, which will be explained in detail using DFT results. Furthermore, the real-space images show how the atoms move and reconfigure on the surface.

To examine the relationship between surface reconstructions and electronic structures of a Mn_3O_4 nanoparticle, EELS spectrum imaging was performed on the Mn_3O_4 nanoparticle standing along the [111] zone axis. In general, core-level excitations tend to shift to higher energies for higher oxidation states, and these chemical shifts are widely used as an indicator for the oxidation state in EELS and XAS. The Mn L_3 edge is one of the edges that clearly shows a monotonic increase with oxidation state.[32] In the case of a mixed-valence Mn_3O_4 compound, the Mn L_3 edge consists of two separate peaks corresponding to the Mn^{2+} and Mn^{3+} states, which are clearly distinguished by a difference in peaks of 1.5 eV.[32−34] The ratio

https://doi.org/10.1021/acs.jpclett.2c01638
J. Phys. Chem. Lett. 2022, 13, 8336−8343

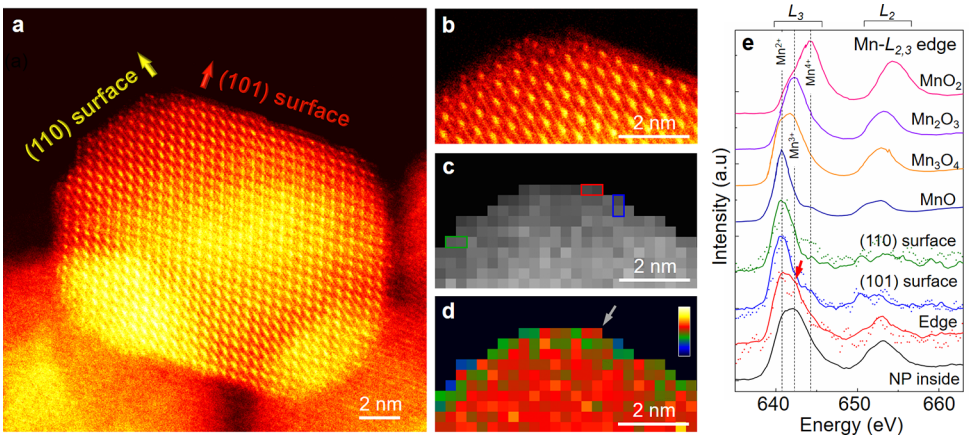

Figure 3. Electronic state of Mn_3O_4 nanoparticle surfaces. (a) High-resolution HAADF STEM image of a nanoparticle viewed along the slightly tilted [100] zone axis. (b) Enlarged experimental image for the edge region in (a), showing regions of interest for electron energy loss spectroscopy (EELS) imaging. (c) HAADF STEM image of Mn_3O_4 nanoparticles, simultaneously acquired during the measurement of the EELS spectrum image. (d) Map of the intensity ratio between Mn^{2+} and Mn^{3+} (I^{3+}/I^{2+}) obtained by the two-Gaussian fitting. (e) EELS spectra of a corresponding color line box in (c) with reference Mn $L_{2,3}$ EELS spectra.[34] The discrete points and solid lines in the EELS spectra of edge, (110), and (101) surfaces indicate the raw EELS data and the postprocessed spectra with principal component analysis, respectively.

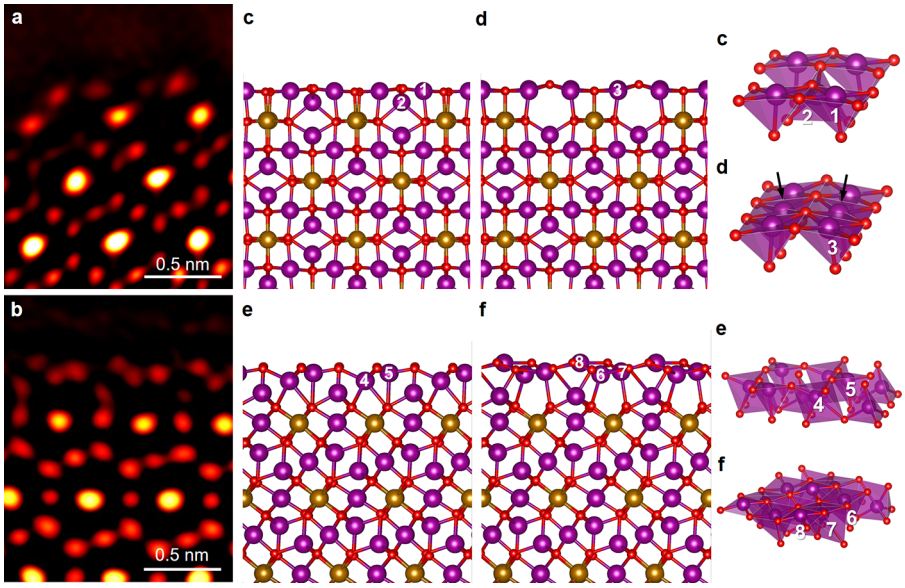

Figure 4. Atomic structure models of the (110) and (101) surfaces relaxed by density functional theory (DFT) calculations. (a,b) Enlarged HAADF STEM images of the (110) and (110) surfaces, respectively. Atomic structure model of the (110) surface: (c) cleaved surface and (d) reconstructed surface. Excess Mn ions present in the reconstructed (110) surface are denoted by the black arrows. Atomic structure model of the (101) surface: (e) cleaved surface and (f) reconstructed surface. The purple and red balls indicate Mn and O ions, respectively. The purple/gold and red balls indicate Mn and O ions, respectively. The Mn ions within high-density atomic columns are denoted by the gold color to distinguish the atomic sites exhibiting a brighter contrast in the HAADF STEM image. The surface Mn ions are individually designated by the number indexes from 1 to 8 for the analysis of on-site *d* orbital occupations (Table 1).

of these two separate peaks at the L_3 edge of the mixed valent Mn_3O_4 varies depending on the ratio of Mn^{2+} and Mn^{3+} ions in the atomic column at the position of the electron probe.[34] Figure 3(a) shows the overall shape of a nanoparticle, and Figure 3(b) shows the region of the nanoparticle where the EELS spectrum imaging was performed. Although atomic columns are not clearly visible in these HAADF STEM images, as the zone axis was slightly tilted, the signatures of surface reconstruction could still be seen in Figure 3(a,b), with bright Mn columns appearing at the topmost layer of the (110) surface and the topmost layer of the (101) surface consisting of only dark Mn columns. Figure 3(c) is an EELS spectrum image taken in the region shown in Figure 3(b).

The shape of the Mn L_3 edge varied significantly near the surface compared to that inside the nanoparticles as shown in Figure 3(e). The change of oxidation states at the surface was investigated by quantitative analysis of the Mn L_3 edge. The L_3 edge at each point of the nanoparticle was fitted with two Gaussian functions centered at 641.0 and 642.5 eV (see Figure S3) to obtain the ratio of Mn^{3+} and Mn^{2+}; here, the two Gaussian functions are assumed to represent the spectral weight of Mn^{2+} and Mn^{3+} peaks, respectively. The intensity ratios of the two Gaussian functions, I^{3+}/I^{2+}, are displayed as a color map in Figure 3(d). Importantly, there was a reduction of the intensity ratio at both the (110) and (101) reconstructed surfaces compared to that inside the nanoparticle. Meanwhile,

https://doi.org/10.1021/acs.jpclett.2c01638
J. Phys. Chem. Lett. 2022, 13, 8336−8343

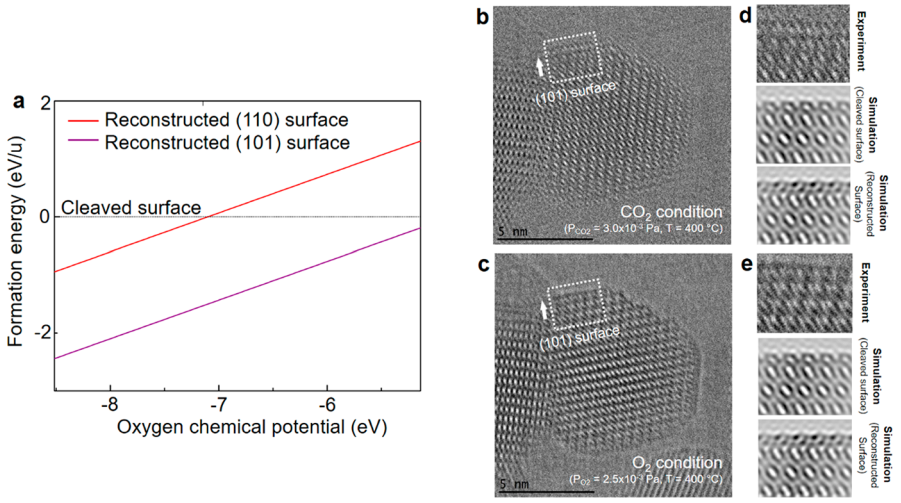

Figure 5. Dependence of oxygen chemical potential on surface structures of Mn_3O_4 nanoparticles. (a) The formation energy of reconstructed surfaces as a function of oxygen chemical potential. The purple and red solid lines indicate the (110) and (101) reconstructed surfaces, respectively. The (110) and (101) cleaved surfaces were chosen as references for the corresponding reconstructed surfaces. (b) Environmental TEM (ETEM) image of a Mn_3O_4 nanoparticle at the CO_2 environment (P_{CO2} of 3.0×10^{-3} Pa) at 400 °C. (c) ETME image of the Mn_3O_4 nanoparticle at the O_2 environment (P_{O2} of 2.5×10^{-3} Pa) at 400 °C. (d) Enlarged image of the (101) surface (marked by a dashed line box in (b)) at the CO_2 environment, and simulated HRTEM images of the cleaved and reconstructed surfaces. (e) Enlarged image of the (101) surface (marked by a dashed line box in (c)) at the O_2 environment, and simulated HRTEM images of the cleaved and reconstructed surfaces.

Table 1. Charge Occupations and Oxidation States of Surface Mn Ions in the Mn_3O_4 Cleaved and Reconstructed Surfaces[a]

	Mn 1 in (110) cleaved surface	Mn 2 in (110) cleaved surface	Mn 3 in (110) reconstructed surface	Mn 4 in (101) cleaved surface	Mn 5 in (101) cleaved surface	Mn 6 in (101) reconstructed surface	Mn 7 in (101) reconstructed surface	Mn 8 in (101) reconstructed surface
f_{Mn}	0.48 0.29 **0.93** 0.12 **0.94** 0.05 **0.95** 0.05 **0.95** 0.04	**0.93** 0.07 **0.93** 0.06 **0.93** 0.05 **0.94** 0.02 **0.94** 0.02	**0.92** 0.11 **0.94** 0.06 **0.94** 0.04 **0.94** 0.03 **0.95** 0.02	0.43 0.34 **0.94** 0.13 **0.95** 0.08 **0.96** 0.07 **0.96** 0.06	0.61 0.31 0.67 0.27 **0.93** 0.13 **0.95** 0.10 **0.96** 0.09	0.68 0.26 **0.94** 0.12 **0.94** 0.06 **0.95** 0.05 **0.96** 0.05	0.84 0.17 **0.92** 0.07 **0.94** 0.05 **0.95** 0.04 **0.95** 0.04	**0.92** 0.12 **0.93** 0.08 **0.93** 0.06 **0.94** 0.04 **0.95** 0.03
	Mn^{3+}	Mn^{2+}	Mn^{2+}	Mn^{3+}	Mn^{3+}	$Mn^{2.5+}$	$Mn^{2.5+}$	Mn^{2+}

[a]Surface Mn ions are designated by the number index marked on the purple balls of the atomic structure models (Figure 4(c–f)). The left and right columns in an eigenoccupation (f_{Mn}) indicate the orbital occupations of majority and minority spins, respectively; f_{Mn} are the eigenvalues of the on-site *d* orbital density matrix of a Mn ion. The occupied, and partially occupied orbitals are denoted in black boldface and red. in the table, respectively. The oxidation state of the Mn ion is estimated by counting the number of occupied orbitals. Mn 1 and 4 ions in (110) and (101) cleaved surfaces are Mn^{3+} ions with a high-spin d_4 configuration; their orbital occupations (i.e., eigenoccupations) are identical to those of Mn^{3+} ions in bulk Mn_3O_4 (see Figure S7).

the intensity ratio did not decrease at the edge of the nanoparticle, which is denoted by the gray arrow in Figure 3(d). This implies that Mn ions preserved the Mn^{3+} states at the edges, in which Mn ionic locations could be relatively easily adjusted, while Mn ions at the reconstructed structures have a significantly reduced valence state. Here, the edge refers to a line segment where two low-index planes meet. These observations were also directly shown in the raw spectra. Figure 3(e) shows the raw Mn $L_{2,3}$ EELS spectra of the region highlighted in Figure 3(c) with the reference spectra. The red-, blue-, and green-highlighted regions indicate parts of the edge, (101) facet, and (110) facet, respectively. As shown in Figure 3(e), the Mn^{3+} peak was fully suppressed in the L_3 spectra of the reconstructed surfaces, whereas it clearly appeared in the spectrum of the edge (see the red solid arrow in Figure 3(e)).

We used DFT calculations to further explore the thermodynamic stability, valence states, and polarity compensation of the (110) and (101) reconstructed surfaces observed in STEM-EELS profile images. Atomic configurations of a cleaved surface and a reconstructed surface of each plane were compared. The cleaved surface was modeled by simply terminating the crystal, while the reconstructed surface was modeled by constructing an atomic structure based on the HAADF STEM image. To reflect the surface reconstruction

https://doi.org/10.1021/acs.jpclett.2c01638
J. Phys. Chem. Lett. 2022, 13, 8336−8343

from the cleaved (110) surface, one Mn atom at the subsurface layer was removed, and two Mn atoms were added into the topmost layer. For the (101) reconstructed surface, one more Mn atom at the specific position of the topmost layer was added. The final structures were obtained by structural relaxations using DFT calculations. Figure 4(c,d) shows the models for the cleaved (110) surface and the reconstructed (110) surface, respectively. Similarly, Figure 4(e,f) represents the models for the cleaved (101) surface and the reconstructed (101) surface, respectively. For further confirmation of the surface structures, multislice HAADF STEM simulations with the experimental parameters were performed. Simulated HAADF STEM images from the reconstructed surface models showed reasonable agreement with the experimental HAADF STEM images (see Figure S4).

To compare the thermodynamic stability of the cleaved and reconstructed surfaces, the formation energy of each surface was calculated. The formation energy cannot be directly compared between the cleaved and reconstructed surfaces, because the surface stoichiometries are not the same. Thus, the surface formation energy was compared as a function of the oxygen chemical potential. As shown in Figure 5(a), the reconstructed surfaces are more stable than the cleaved surface for a large range of oxygen chemical potentials. However, according to the numerical results, the cleaved surfaces are expected to be stabilized under oxygen-rich conditions. To verify the dependence of surface structures on the oxygen chemical potentials, environmental TEM (ETEM) experiments were carried out for the same nanoparticles. Figure 5(b,c) shows the ETEM images measured at the CO_2- and O_2-gas conditions, respectively. Interestingly, the atomic arrangement of the (101) surface was changed depending on the gas environment; the reconstructed surface model matches well with the experimental image of the (101) surface in the CO_2-gas environment, while the cleaved surface model is consistent with the image in the O_2-gas environment. These ETEM results verify our understanding of the oxygen-chemical-potential dependence of surface reconstruction.

The role of surface reconstructions on the valence state and polar instability was further studied by analyzing the orbital configurations of Mn ions at the surfaces. The charge and orbital states of Mn ions can be directly determined by the eigenoccupation (f_{Mn}) of the on-site d orbital density matrix; f_{Mn} of surface Mn ions is summarized in Table 1.[35−37] To be specific, the oxidation state of each Mn ion on the surface was estimated by counting the number of occupied orbitals (i.e., the number of occupied eigenstates). The eigenorbital and eigenoccupations are fictitious auxiliary physical quantities, but they have been widely used in the analysis of orbital-dependent physical phenomena. The analysis of these orbital states suggests that Jahn−Teller as well as polar instabilities were mitigated by the surface reconstructions. As shown in Table 1, there was no Mn^{3+} ion with a high-spin d_4 configuration on the top-surface layer of both reconstructed surfaces; instead, the reconstructed (110) surface was composed of closely packed Mn^{2+} ions, and the reconstructed (101) surface consists of $Mn^{2.5+}$ ions with Mn^{2+} ions intercalated periodically in the middle. On the other hand, Mn^{3+} ions remained on the top-surface layer of the cleaved surface models. These numerical results indicate that the Jahn−Teller instability associated with Mn^{3+} is relieved in the atomic configuration of the reconstructed surfaces. Moreover, we estimated the net charge and surface polarization of the top-surface layer using the numerically derived oxidation state (see Figure S5). The top-surface layer of the (110) surface became neutral through the surface reconstruction, and the polarity of the (101) surface was also weakened as additional Mn ions were periodically embedded into the uppermost oxygen layer. Theoretical confirmation of the polarity compensation in the reconstructed surface again explains the need for the surface reconstruction, as suggested in previous studies. Note that the features of the reconstructed surface surrounded by Mn^{2+} ions are in good agreement with the EELS spectrum imaging, showing that the I^{3+}/I^{2+} of the surface was lower than inside the nanoparticles.

These results, i.e., STEM-EELS measurements and DFT calculations, provide direct insights into the excellent catalytic activity of Mn_3O_4 in a nanostructure. Importantly, Mn^{3+} ions, which are known to act as the active sites, were suppressed on the (110) and (101) facets because of surface reconstructions. Mn^{3+} ions were still exposed at the edge of the nanoparticle, explaining why Mn_3O_4 was highly active in the form of nanoparticles. Nanoparticles have a much higher concentration of edges, corners, and high-index facets with decreasing size; e.g., the ratio of edges to volume is inversely proportional to the square of particle size. Meanwhile, we recognized that the surfaces of Mn_3O_4 nanoparticles are continuously and gradually evolved through the chemical reaction (see Figure S6). Therefore, further *in situ* or *ex situ* STEM-EELS works are desirable to examine surface evolution and its influences on the catalytic properties of Mn_3O_4 nanoparticles. Still, we expect that the surface reconstruction of low-index facets will often occur even in reaction environment to mitigate polar and Jahn−Teller instabilities.

By using STEM-EELS profile imaging and DFT calculations, we showed that the activity of the Mn_3O_4 nanoparticle can be enhanced at edges, corners, or high-index facets whereas suppressed at reconstructed low-index facets. Stable low-index surfaces of Mn_3O_4 nanoparticles are found to be easily reconstructed to mitigate the polar and Jahn−Teller instabilities. Importantly, Mn^{3+} ions, which are strongly coupled to the active sites in OER, are largely converted into ions with different chemical states in the reconstructed surfaces, while they are still observed at the edges of nanoparticles. Our results directly demonstrate that surface reconstructions can deactivate the active sites in Mn-based OER catalysts. In addition, this study further suggests that the disturbance of surface reconstructions, e.g., via surface doping or vacancy formation, can be a promising strategy to enhance their catalytic activities.

■ ASSOCIATED CONTENT

Supporting Information

The Supporting Information is available free of charge at https://pubs.acs.org/doi/10.1021/acs.jpclett.2c01638.

Experimental and computational methods (including synthesis, STEM-EELS measurements, ETEM experiments, and DFT calculations), additional high-resolution HAADF STEM images of Mn_3O_4 nanoparticles, details on two Gaussian-function fittings of EELS spectra, simulated HAADF STEM images of the (110) and (101) surfaces, estimation of polarity for the (110) and (101) surfaces, XPS spectra of Mn_3O_4 nanoparticles before and after OER, orbital occupation of Mn^{2+} and

https://doi.org/10.1021/acs.jpclett.2c01638
J. Phys. Chem. Lett. 2022, 13, 8336−8343

Mn^{3+} in bulk Mn_3O_4, and XRD spectra of Mn_3O_4 nanoparticles (PDF)

AUTHOR INFORMATION

Corresponding Author

Miyoung Kim − *Department of Materials Science and Engineering, Seoul National University, Seoul 08826, Republic of Korea;* orcid.org/0000-0001-8632-6711; Email: mkim@snu.ac.kr

Authors

Sangmoon Yoon − *Department of Materials Science and Engineering, Seoul National University, Seoul 08826, Republic of Korea; Department of Physics, Gachon University, Seongnam, Gyeonggi-do 13120, Republic of Korea*

Hongmin Seo − *Department of Materials Science and Engineering, Seoul National University, Seoul 08826, Republic of Korea*

Kyoungsuk Jin − *Department of Materials Science and Engineering, Seoul National University, Seoul 08826, Republic of Korea; Department of Chemistry and Research Institute for Natural Sciences, Korea University, Seoul 02841, Republic of Korea*

Hyoung Gyun Kim − *Department of Materials Science and Engineering, Seoul National University, Seoul 08826, Republic of Korea*

Seung-Yong Lee − *Department of Materials Science and Engineering, Seoul National University, Seoul 08826, Republic of Korea; Division of Materials Science and Engineering, Hanyang University, Seoul 04763, Republic of Korea*

Janghyun Jo − *Department of Materials Science and Engineering, Seoul National University, Seoul 08826, Republic of Korea*

Kang Hee Cho − *Department of Materials Science and Engineering, Seoul National University, Seoul 08826, Republic of Korea*

Jinseok Ryu − *Department of Materials Science and Engineering, Seoul National University, Seoul 08826, Republic of Korea;* orcid.org/0000-0002-9558-3469

Aram Yoon − *Department of Materials Science and Engineering, University of Illinois, Urbana−Champaign, Illinois 61801, United States*

Young-Woon Kim − *Department of Materials Science and Engineering, Seoul National University, Seoul 08826, Republic of Korea*

Jian-Min Zuo − *Department of Materials Science and Engineering, University of Illinois, Urbana−Champaign, Illinois 61801, United States;* orcid.org/0000-0002-5151-3370

Young-Kyun Kwon − *Department of Physics, Department of Information Display, and Research Institute for Basic Sciences, Kyung Hee University, Seoul 02447, Republic of Korea;* orcid.org/0000-0001-6027-8408

Ki Tae Nam − *Department of Materials Science and Engineering, Seoul National University, Seoul 08826, Republic of Korea;* orcid.org/0000-0001-6353-8877

Complete contact information is available at: https://pubs.acs.org/10.1021/acs.jpclett.2c01638

Author Contributions

S.Y., K.T.N., and M.K. initiated the project. S.Y. performed STEM-EELS experiments and DFT calculations. H.S., K.J., and K.H.C. conducted synthesis and electrochemical testing under supervision of K.T.N. H.G.K. and A.Y. carried out ETEM experiments under supervision of J.-M.Z. S.Y. analyzed the data with help from K.J., S.-Y.L., J.J., J.R., Y.-W.K., Y.-K.K., and M.K. S.Y. and M.K. wrote the manuscript. All authors discussed and commented critically on the manuscript. M.K. supervised the whole project.

Notes

The authors declare no competing financial interest.

ACKNOWLEDGMENTS

We acknowledge financial support from the Korean government through the National Research Foundation (2022R1A2C3007807, 2022R1A2C1005505, 2022R1F1A1072330, 2022R1C1C1010157). STEM-EELS measurement was supported by the National Center for Inter-University Research Facilities (NCIRF) at Seoul National University in Korea.

ABBREVIATIONS

STEM	scanning transmission electron microscopy
EELS	electron energy loss spectroscopy
DFT	density functional theory
OER	oxygen evolution reaction
SAED	selected area electron diffraction
FFT	fast Fourier transformation
CV	cyclic voltammetry

REFERENCES

(1) Somorjai, G. A.; Li, Y.*Introduction to Surface Chemistry and Catalysis*, 2nd ed.; John Wiley & Sons, 2010.

(2) Ertl, G. Reactions at Surfaces: From Atoms to Complexity (Nobel Lecture). *Angewandte Chemie - International Edition* **2008**, *47*, 3524−3535.

(3) Jaramillo, T. F.; Jørgensen, K. P.; Bonde, J.; Nielsen, J. H.; Horch, S.; Chorkendorff, I. Identification of Active Edge Sites for Electrochemical H2 Evolution from Mos2 Nanocatalysts. *Science* **2007**, *317*, 100−102.

(4) Buurmans, I. L. C.; Weckhuysen, B. M. Heterogeneities of Individual Catalyst Particles in Space and Time as Monitored by Spectroscopy. *Nat. Chem.* **2012**, *4*, 873−886.

(5) Marks, L. D.; Smith, D. J. Direct Surface Imaging in Small Metal Particles. *Nature* **1983**, *303*, 316−317.

(6) Cowley, J. M. Electron Microscopy of Surface Structure. *Prog. Surf. Sci.* **1986**, *21*, 209−250.

(7) Shibata, N.; Goto, A.; Choi, S. Y.; Mizoguchi, T.; Findlay, S. D.; Yamamoto, T.; Ikuhara, Y. Direct Imaging of Reconstructed Atoms on Tio2 (110) Surfaces. *Science* **2008**, *322*, 570−573.

(8) Yu, R.; Hu, L. H.; Cheng, Z. Y.; Li, Y. D.; Ye, H. Q.; Zhu, J. Direct Subangstrom Measurement of Surfaces of Oxide Particles. *Phys. Rev. Lett.* **2010**, *105*, 226101.

(9) Lin, Y.; Wen, J.; Hu, L.; Kennedy, R.; Stair, P. C.; Poeppelmeier, K. R.; Marks, L. D. Synthesis-Dependent Atomic Surface Structures of Oxide Nanoparticles. *Phys. Rev. Lett.* **2013**, *111*, 156101.

(10) Wintterlin, J.; Schuster, R.; Ertl, G. Existence of a "Hot" Atom Mechanism for the Dissociation of O2 on Pt(111). *Phys. Rev. Lett.* **1996**, *77*, 123−126.

(11) Over, H.; Kim, Y. D.; Seitsonen, A. P.; Wendt, S.; Lundgren, E.; Schmid, M.; Varga, P.; Morgante, A.; Ertl, G. Atomic-Scale Structure and Catalytic Reactivity of the Ruo2(110) Surface. *Science* **2000**, *287*, 1474−1476.

(12) De Smit, E.; et al. Nanoscale Chemical Imaging of a Working Catalyst by Scanning Transmission X-Ray Microscopy. *Nature* **2008**, *456*, 222−225.
(13) Shapiro, D. A.; et al. Chemical Composition Mapping with Nanometre Resolution by Soft X-Ray Microscopy. *Nat. Photonics* **2014**, *8*, 765−769.
(14) Stavitski, E.; Weckhuysen, B. M. Infrared and Raman Imaging of Heterogeneous Catalysts. *Chem. Soc. Rev.* **2010**, *39*, 4615−4625.
(15) Wu, C. Y.; Wolf, W. J.; Levartovsky, Y.; Bechtel, H. A.; Martin, M. C.; Toste, F. D.; Gross, E. High-Spatial-Resolution Mapping of Catalytic Reactions on Single Particles. *Nature* **2017**, *541*, 511−515.
(16) Van Schrojenstein Lantman, E. M.; Deckert-Gaudig, T.; Mank, A. J. G.; Deckert, V.; Weckhuysen, B. M. Catalytic Processes Monitored at the Nanoscale with Tip-Enhanced Raman Spectroscopy. *Nat. Nanotechnol.* **2012**, *7*, 583−586.
(17) Ferreira, K. N.; Iverson, T. M.; Maghlaoui, K.; Barber, J.; Iwata, S. Architecture of the Photosynthetic Oxygen-Evolving Center. *Science* **2004**, *303*, 1831−1838.
(18) Jin, K.; et al. Partially Oxidized Sub-10 Nm Mno Nanocrystals with High Activity for Water Oxidation Catalysis. *Sci. Rep.* **2015**, *5*, 10279.
(19) Yu, M. Q.; Li, Y. H.; Yang, S.; Liu, P. F.; Pan, L. F.; Zhang, L.; Yang, H. G. Mn3o4 Nano-Octahedrons on Ni Foam as an Efficient Three-Dimensional Oxygen Evolution Electrocatalyst. *Journal of Materials Chemistry A* **2015**, *3*, 14101−14104.
(20) Zaharieva, I.; Chernev, P.; Risch, M.; Klingan, K.; Kohlhoff, M.; Fischer, A.; Dau, H. Electrosynthesis, Functional, and Structural Characterization of a Water-Oxidizing Manganese Oxide. *Energy Environ. Sci.* **2012**, *5*, 7081−7089.
(21) Indra, A.; Menezes, P. W.; Zaharieva, I.; Baktash, E.; Pfrommer, J.; Schwarze, M.; Dau, H.; Driess, M. Active Mixed-Valent Mnox Water Oxidation Catalysts through Partial Oxidation (Corrosion) of Nanostructured Mno Particles. *Angewandte Chemie - International Edition* **2013**, *52*, 13206−13210.
(22) Park, J.; et al. A New Water Oxidation Catalyst: Lithium Manganese Pyrophosphate with Tunable Mn Valency. *J. Am. Chem. Soc.* **2014**, *136*, 4201−4211.
(23) Takashima, T.; Hashimoto, K.; Nakamura, R. Inhibition of Charge Disproportionation of Mno2 Electrocatalysts for Efficient Water Oxidation under Neutral Conditions. *J. Am. Chem. Soc.* **2012**, *134*, 18153−18156.
(24) Takashima, T.; Hashimoto, K.; Nakamura, R. Mechanisms of Ph-Dependent Activity for Water Oxidation to Molecular Oxygen by Mno2 Electrocatalysts. *J. Am. Chem. Soc.* **2012**, *134*, 1519−1527.
(25) Robinson, D. M.; Go, Y. B.; Mui, M.; Gardner, G.; Zhang, Z.; Mastrogiovanni, D.; Garfunkel, E.; Li, J.; Greenblatt, M.; Dismukes, G. C. Photochemical Water Oxidation by Crystalline Polymorphs of Manganese Oxides: Structural Requirements for Catalysis. *J. Am. Chem. Soc.* **2013**, *135*, 3494−3501.
(26) Roger, I.; Shipman, M. A.; Symes, M. D. Earth-Abundant Catalysts for Electrochemical and Photoelectrochemical Water Splitting. *Nature Reviews Chemistry* **2017**, *1*, 0003.
(27) Cho, K. H.; Seo, H.; Park, S.; Lee, Y. H.; Lee, M. Y.; Cho, N. H.; Nam, K. T. Uniform, Assembled 4 Nm Mn3o4 Nanoparticles as Efficient Water Oxidation Electrocatalysts at Neutral Ph. *Adv. Funct. Mater.* **2020**, *30*, 1910424.
(28) Kanan, M. W.; Nocera, D. G. In-Situ Formation of an Oxygen-Evolving Catalyst in Neutral Water Containing Phosphate and Co2+. *Science* **2008**, *321*, 1072.
(29) Lee, Y. H.; Park, S.; Lee, K. G.; Lee, M. Y.; Cho, K. H.; Kim, S. J.; Nam, K. T. Methylamine Treated Mn3o4 Nanoparticles as a Highly Efficient Water Oxidation Catalyst under Neutral Condition. *ChemCatChem.* **2019**, *11*, 1665−1672.
(30) Yoon, S.; Ok, J. M.; Lee, S. A.; Lee, J.; Huon, A.; Lupini, A. R.; Choi, W. S.; Lee, H. N. Atomic Structure of the Initial Nucleation Layer in Hexagonal Perovskite Baruo3 Thin Films. *Advanced Materials Interfaces* **2021**, *8*, 2100023.
(31) Yoon, S.; Gao, X.; Ok, J. M.; Liao, Z.; Han, M.-G.; Zhu, Y.; Ganesh, P.; Chisholm, M. F.; Choi, W. S.; Lee, H. N. Strain-Induced Atomic-Scale Building Blocks for Ferromagnetism in Epitaxial Lacoo3. *Nano Lett.* **2021**, *21*, 4006−4012.
(32) Tan, H.; Turner, S.; Yücelen, E.; Verbeeck, J.; Van Tendeloo, G. 2d Atomic Mapping of Oxidation States in Transition Metal Oxides by Scanning Transmission Electron Microscopy and Electron Energy-Loss Spectroscopy. *Phys. Rev. Lett.* **2011**, *107*, 107602.
(33) Garvie, L. A. J.; Craven, A. J. High-Resolution Parallel Electron Energy-Loss Spectroscopy of Mn L2,3-Edges in Inorganic Manganese Compounds. *Physics and Chemistry of Minerals* **1994**, *21*, 191−206.
(34) Tan, H.; Verbeeck, J.; Abakumov, A.; Van Tendeloo, G. Oxidation State and Chemical Shift Investigation in Transition Metal Oxides by Eels. *Ultramicroscopy* **2012**, *116*, 24−33.
(35) Mellan, T. A.; Corà, F.; Grau-Crespo, R.; Ismail-Beigi, S. Importance of Anisotropic Coulomb Interaction in Lamno3. *Phys. Rev. B* **2015**, *92*, 085151.
(36) Yoon, S.; Jin, K.; Lee, S.; Nam, K. T.; Kim, M.; Kwon, Y.-K. Effects of Paramagnetic Fluctuations on the Thermochemistry of Mno (100) Surfaces in the Oxygen Evolution Reaction. *Phys. Chem. Chem. Phys.* **2021**, *23*, 859−865.
(37) Yoon, S.; Lee, S.; Pang, S.; Kim, M.; Kwon, Y.-K. Role of Anisotropic Coulomb Interactions in the Superexchange Coupling of Mixed-Valent Mn 3 O 4. *Phys. Rev. B* **2021**, *104*, 035158.

https://doi.org/10.1021/acs.jpclett.2c01638
J. Phys. Chem. Lett. 2022, 13, 8336−8343